Materials Advances

ROYAL SOCIETY OF CHEMISTRY

PAPER

View Article Online
View Journal | View Issue

Cite this: *Mater. Adv.*, 2023, 4, 1345

Mechanism of ionic polarizability, bond valence, and crystal structure on the microwave dielectric properties of disordered $Li_{10}MTi_{13}O_{32}$ (M = Zn, Mg) spinels†

Ying Tang,*[a] Mu Li,[b] Huaicheng Xiang,*[a] Jie Li,[b] Yuandong Qin[d] and Liang Fang[bc]

Received 10th December 2022,
Accepted 6th February 2023

DOI: 10.1039/d2ma01074g

rsc.li/materials-advances

The influence mechanism of the microwave dielectric properties of disordered spinels ($Fd\bar{3}m$) $Li_{10}MTi_{13}O_{32}$ (M = Zn, Mg) was investigated *via* Rietveld structural refinement, ionic polarizability, bond valence, P–V–L theory, Raman spectroscopy, and DC conductivity. For $Li_{10}ZnTi_{13}O_{32}$ and $Li_{10}MgTi_{13}O_{32}$, promising microwave dielectric properties of ε_r = 28.23 ± 0.3 and 29.23 ± 0.3, $Q \times f$ = 35 800 ± 500 GHz and 32 100 ± 500 GHz (at ~7.5 GHz), and τ_f = −17.06 ± 2.0 ppm per °C and −11.05 ± 2.0 ppm per °C, respectively, were obtained at 980 °C. Bond valences reveal that almost all cations are rattling, weakening the bond strengths and widening the molecular dielectric polarizability. The expansion structures also result in τ_f values closer to zero and lower $Q \times f$ values. The bond ionicity and lattice energy of the Ti–O bonds are much greater than those of other bonds, indicating that the Ti–O bond is a major contributor to ε_r and $Q \times f$. Moreover, the DC conductivity clarified that the $Q \times f$ values of the disordered spinels $Li_{10}ZnTi_{13}O_{32}$ and $Li_{10}MgTi_{13}O_{32}$ are not as high as other ordered spinels because of the transport of Li^+ ions in their structures.

1. Introduction

From 1G to 5G (the fifth generation mobile network), mobile communications are constantly expanding towards higher frequency bands (microwave, millimeter wave and centimeter wave) to increase speed and capacity, which is inseparable from the support of microwave dielectric ceramic materials. Microwave dielectric ceramics for 5G applications need to have a low relative permittivity (ε_r) for modulating signal delay, a high quality factor ($Q \times f$) to suppress signal attenuation, and a near-zero temperature coefficient of resonance frequency (τ_f) to ensure device stability in high-temperature environments.[1–6]

Microwave dielectric ceramics with a spinel structure (AB_2O_4), such as $MgAl_2O_4$,[7–9] and Mg_2TiO_4,[10] have been reported to possess a relatively low ε_r and a high $Q \times f$. In order to overcome the high sintering temperature, τ_f is not close to zero for traditional spinels, so a large number of Li-containing spinels have been reported, such as $Li_2ATi_3O_8$ (A = Zn, Mg),[11,12] $LiGa_5O_8$,[13,14] $Li_2Zn_3Ti_4O_{12}$,[15] and $Li_4Ti_5O_{12}$.[16–18] Concerning the Li_2O–AO–TiO_2 (A = Zn, Mg) systems, recent studies have focused on the characterization and microwave dielectric properties of two ordered ceramics of $Li_2ZnTi_3O_8$ (ε_r = 25.6–26.2, $Q \times f$ = 62 000–72 000 GHz, and τ_f = −15 to −11.2 ppm per °C) and $Li_2MgTi_3O_8$ (ε_r = 20.2, $Q \times f$ = 42 000 GHz, and τ_f = +3.2 ppm per °C), but the microwave dielectric properties of disordered spinel ceramics have rarely been reported. For ordered Li-containing spinels, Li_{4b} and Ti_{12d} at the octahedral sites were arranged spontaneously into 1 : 3 cation ordering (*i.e.*, $[Li_{0.5}Zn_{0.5}]^{tet}[Li_{0.5}Ti_{1.5}]^{oct}O_4$ and $[Li_{0.55}Mg_{0.45}]^{tet}[(Li_{0.45}Mg_{0.05})$-$Ti_{1.5}]^{oct}O_4$) with a space group of $P4_332$. The spinel-structured $Li_2MM'_3O_8$ (M = Mg, Co, Ni, Zn; M′ = Ti, Ge) ceramics with an ordered spinel structure ($P4_332$) have been reported to possess a relative ε_r of 10.5–28.9, a $Q \times f$ of 47 400–160 000 GHz, and a τ_f of −63.9 to +7.4 ppm per °C.[19–25]

Recently, we found an interesting phenomenon in the ordered spinels $Li_{1.33x}A_{2-2x}Ti_{1+0.67x}O_4$ (x = 0.5625; A = Zn, Mg),[26] namely, a large positive deviation [$\Delta\varepsilon_r = (\varepsilon_{r(corr)}-\varepsilon_{r(C-M)})/\varepsilon_{r(C-M)}$ = 16–91%] between the porosity-corrected permittivity $\varepsilon_{r(corr)}$ and the calculated $\varepsilon_{r(C-M)}$ using the Clausius–Mossotti (C–M) equation, which

[a] College of Science, Guilin University of Technology, Guilin, 541004, China. E-mail: tangyinggl001@aliyun.com, xianghc@glut.edu.cn
[b] Guangxi Universities Key Laboratory of Non-Ferrous Metal Oxide Electronic Functional Materials and Devices, College of Materials Science and Engineering, Guilin University of Technology, Guilin, 541004, China
[c] College of Materials and Chemical Engineering, Key Laboratory of Inorganic Nonmetallic Crystalline and Energy Conversion Materials, China Three Gorges University, Yichang 443002, China
[d] Guangxi New Future Information Industry Co., Ltd., Beihai 536000, China

† Electronic supplementary information (ESI) available. See DOI: https://doi.org/10.1039/d2ma01074g

might be related to the combined effect of the rattling and the compressed cations at the A and B sites, which was mutually verified in garnet and zircon systems,[27–30] thus establishing the interaction mechanism of bond length, polarization, permittivity, and τ_f.

Hernandez *et al.*[31] discovered that $Li_{1.33x}Zn_{2-2x}Ti_{1+0.67x}O_4$ spinels undergo two order–disorder transitions to the interval of x = [0–1], where $x \leq 0.5$ is the disordered face-centered cubic phase ($Fd\bar{3}m$), $0.5 < x < 0.9$ is the ordered primitive cubic phase ($P4_332$), and when x is beyond 0.9, it becomes face-centered cubic again. And a similar phenomenon occurs in magnesium analogs.[32] The different cation occupation is the main reason for the order and disorder changes in the spinel structure. In the disordered structure, there is only one kind of regular octahedron (16d) and one tetrahedron (8a), compared with the two octahedra (4b, 12d) and one tetrahedron (8c) in the ordered structure. The disordered structure is simpler and more conducive to studying the influence of the bond length, bond valence, and polarization on the microwave dielectric properties.

In this paper, we focus on the disordered compositions $Li_{10}MTi_{13}O_{32}$ (M = Zn, Mg) with x = 0.9375 in $Li_{1.33x}M_{2-2x}Ti_{1+0.67x}O_4$ spinels. It is a Z = 1 structure located between the disorder x = 0.9 and x = 1 ($Li_4Ti_5O_{12}$, ε_r = 30.1, $Q \times f$ = 29 530 GHz, τ_f = −15 ppm per °C).[13] The main aim of this work is to investigate the effects of the bond length, bond valence, ionic dielectric polarizability, structural stability, and rattling and compressed cations on the microwave dielectric properties (ε_r, τ_f, and $Q \times f$) both theoretically and experimentally.

2. Experimental procedure

$Li_{10}MTi_{13}O_{32}$ (M = Zn, Mg) ceramics were prepared *via* a solid-state reaction using high-purity (>99.99%) Li_2CO_3, ZnO, MgO, and TiO_2 (rutile) powders as raw materials. Before weighing, the MgO, ZnO, and TiO_2 powders were calcined to remove any moisture (900 °C/2 h). The raw materials were ground using a ball mill for 6 h, the powder was calcined at 800 °C for 4 h, and then it was ball milled once with a 5 wt% PVA binder. The obtained powder was uniaxially pressed into cylinders with a diameter of 10 mm and a height of 5 mm at a pressure of 150 MPa. Subsequently, the samples were heated from room temperature to 550 °C for 4 h to burn off the organic binder and then sintered at 940–1020 °C for 4 h with a temperature-ramping rate of 5 °C min^{-1}.

The phase purity and crystal structure of the $Li_{10}MTi_{13}O_{32}$ (M = Zn, Mg) ceramics were identified *via* a powder X-ray diffractometer (X'Pert PRO). Scanning electron microscopy (SEM; S4800, Hitachi) was used to observe the grain growth of the $Li_{10}MTi_{13}O_{32}$ (M = Zn, Mg) ceramics after polishing and thermal etching (below the sintering temperature of 50 °C for 30 min). The average grain size of the $Li_{10}MTi_{13}O_{32}$ (M = Zn, Mg) ceramics was evaluated using Nano Measurer software. The densities of the sintered ceramics were determined using the Archimedes principle. The Raman spectra of the ceramics were collected using a Raman spectrometer (Thermo Fisher Scientific) with a 532 nm laser. Impedance spectroscopy was carried out using an impedance analyzer (4291A, Agilent, America), and DC conductivity testing was performed using a high-temperature resistivity test system (RMS-1000I, Partulab, China) at selected temperatures. The ε_r, dielectric loss ($\tan\delta = 1/Q$), and resonant frequency (f) were determined using the Hakki–Coleman method using a network analyzer (N5230A, Agilent, America) (ESI†). The drift of the f and ε_r (*i.e.*, τ_f and τ_ε) were calculated as follows:

$$\tau_f = \frac{f_2 - f_1}{f_1 \times (T_2 - T_1)} \quad (1)$$

$$\tau_\varepsilon = \frac{\varepsilon_{r2} - \varepsilon_{r1}}{\varepsilon_{r1} \times (T_2 - T_1)} \quad (2)$$

where f_1 and f_2 represent the resonant frequency at T_1 and T_2, respectively.

3. Results and discussion

Fig. 1a shows the XRD patterns of the $Li_{10}ZnTi_{13}O_{32}$ and $Li_{10}MgTi_{13}O_{32}$ ceramics sintered at 980 °C, respectively. The diffraction peaks of $Li_{10}MTi_{13}O_{32}$ (M = Zn, Mg) were well indexed with the disordered spinel $Li_4Ti_5O_{12}$ phase (PDF#49-0207). Then, Rietveld structural refinements were carried out on $Li_{10}MTi_{13}O_{32}$ (M = Zn, Mg) established on the reported cubic $Li_4Ti_5O_{12}$ disordered structure model (ICSD#160655) with the space group of $Fd\bar{3}m$. The refined plots for $Li_{10}ZnTi_{13}O_{32}$ and $Li_{10}MgTi_{13}O_{32}$ are displayed in Fig. 1b and c, respectively, and the refined structural parameters are listed in Table 1. It is notable that the refined lattice parameters of a = 8.3636 Å and V = 585.0211 $Å^3$ for $Li_{10}ZnTi_{13}O_{32}$ are smaller than a = 8.3649 Å and V = 585.2944 $Å^3$ for $Li_{10}MgTi_{13}O_{32}$, which is opposite to the ionic radii of Zn^{2+} (0.60 Å) and Mg^{2+} (0.57 Å, CN = 4), which might be related to the rattling effect of cations in $Li_{10}MgTi_{13}O_{32}$. The crystal structure and cation occupancy information of the $Li_{10}MTi_{13}O_{32}$ ceramics are presented in Fig. 1d and Table 1, respectively. It is observed that Li and M share the tetrahedral sites (8a), and Li and Ti share the octahedral sites (16d). The octahedra and tetrahedra are connected at their common vertices, and the octahedra are connected at their common edges to form the structural skeleton. The tetrahedra are isolated from each other, indicating that the influence of the octahedron on the structure is dominant. Moreover, Fig. S1 (ESI†) depicts the bond lengths in $Li_{10}MTi_{13}O_{32}$ (M = Zn, Mg) from the Rietveld refinements.

Raman spectra can reflect the vibrations of chemical bonds and their structural characteristics. The Raman spectra of the $Li_{10}ZnTi_{13}O_{32}$ and $Li_{10}MgTi_{13}O_{32}$ ceramics are shown in Fig. 2. Six modes at 228, 258, 342, 417, 512, and 675 cm^{-1} for $Li_{10}ZnTi_{13}O_{32}$ and 231, 260, 340, 418, 514, and 676 cm^{-1} for $Li_{10}MgTi_{13}O_{32}$ were observed, which are very close to the previously reported values for disordered $Li_4Ti_5O_{12}$ (246, 274, 360, 429, and 680 cm^{-1}; $A_{1g} + E_g + 3F_{2u}$).[33,34] However, the Raman spectra of $Li_{10}ZnTi_{13}O_{32}$ and $Li_{10}MgTi_{13}O_{32}$ show a new

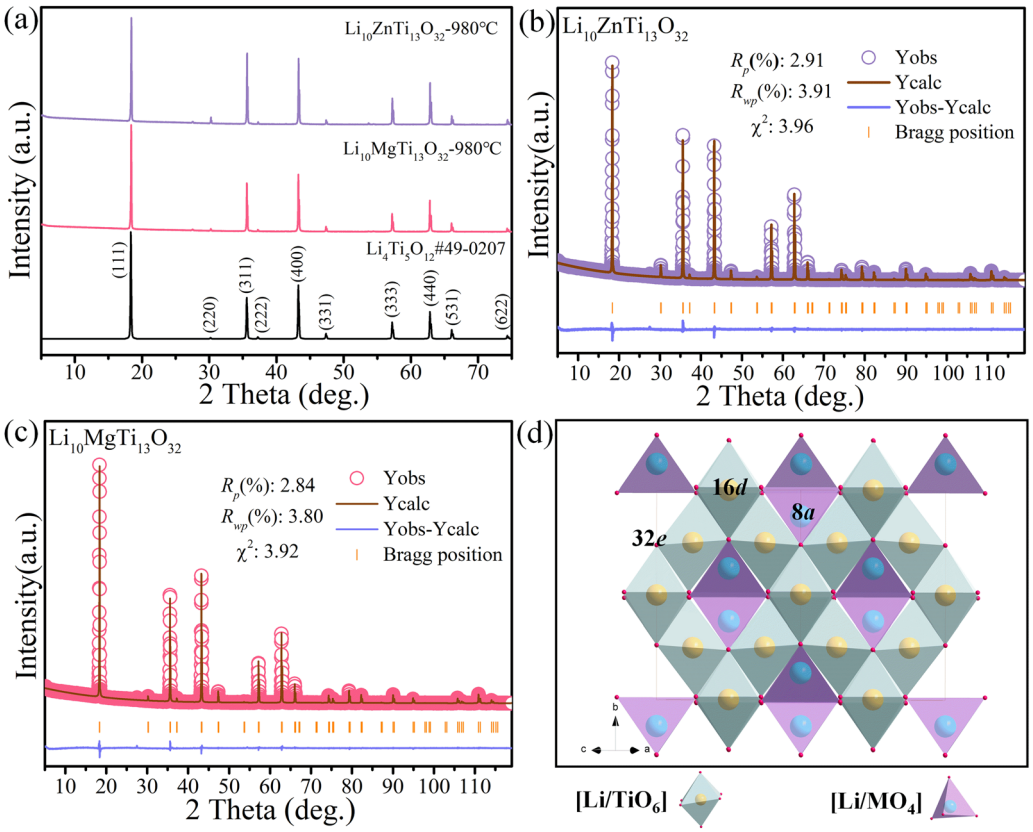

Fig. 1 (a) XRD patterns of the $Li_{10}MTi_{13}O_{32}$ (M = Zn, Mg) ceramics sintered at the optimum temperature. Rietveld refinement patterns of (b) $Li_{10}ZnTi_{13}O_{32}$ and (c) $Li_{10}MgTi_{13}O_{32}$. (d) Schematic diagram of the crystal structure of spinel-type $Li_{10}MTi_{13}O_{32}$ (M = Zn, Mg).

Table 1 Refined structural parameters, thermal parameters, and reliability factors of the $Li_{10}MTi_{13}O_{32}$ (M = Zn, Mg) ceramics

Compound	Atom	Site	Occ.	*x*, *y*, *z*	*B* (Å^2)	*a* (Å)	*V* (Å^3)	R_p (%)	R_{wp} (%)	χ^2
$Li_{10}ZnTi_{13}O_{32}$	Zn(1)	8a	0.1250	0.1250	0.3866	8.3636	585.0211	2.91	3.91	3.96
	Li(1)	8a	0.8750	0.1250	0.3866					
	Li(2)	16d	0.1875	0.5000	0.5396					
	Ti(1)	16d	0.8125	0.5000	0.5396					
	O(1)	32e	1.0000	0.2621	0.4660					
$Li_{10}MgTi_{13}O_{32}$	Mg(1)	8a	0.1250	0.1250	0.5066	8.3649	585.2944	2.84	3.80	3.92
	Li(1)	8a	0.8750	0.1250	0.5066					
	Li(2)	16d	0.1875	0.5000	0.8772					
	Ti(1)	16d	0.8125	0.5000	0.8772					
	O(1)	32e	1.0000	0.2622	0.7794					

mode at 512 cm^{-1} and 514 cm^{-1}, respectively, which may be ascribable to Zn–O and Mg–O stretches in the [ZnO_4] and [MgO_4] tetrahedra.[35,36] For $Li_{10}ZnTi_{13}O_{32}$, the Raman band at 676 cm^{-1} is considered to be the A_{1g} mode associated with the stretching vibration of [TiO_6]. The 417 cm^{-1} band is roughly the E_g mode associated with the [LiO_4] stretching vibration. The mode at 340 cm^{-1} is due to the bending vibrations at the O–Li–O and O–Ti–O bonds. The same is true for the $Li_{10}MgTi_{13}O_{32}$ ceramic, and the Raman vibration modes are listed in Table 2. In addition, most of the Raman shifts of $Li_{10}MgTi_{13}O_{32}$ were found to be lower than those of $Li_{10}ZnTi_{13}O_{32}$, which may be related to the expansion of the cationic-oxygen bond and its larger unit cell parameter (*a*). In general, an increase in bond expansion is accompanied by a weakening of the bond, which leads to a decrease in the frequency.[37]

In the sintering behavior of ceramics, grain growth is a manifestation of the densification process. SEM was carried out to observe the polished and thermally etched grains. As shown in Fig. 3a–c, the average grain size ($\bar{D}$) of $Li_{10}ZnTi_{13}O_{32}$ increased from 3.81 μm to 5.06 μm as the sintering temperature was increased. When sintered at 940 °C, the grain size was not uniform, and there was some slight porosity. As the temperature was increased to 980 °C, the grain size increased with the disappearance of the pores, and the microstructure became

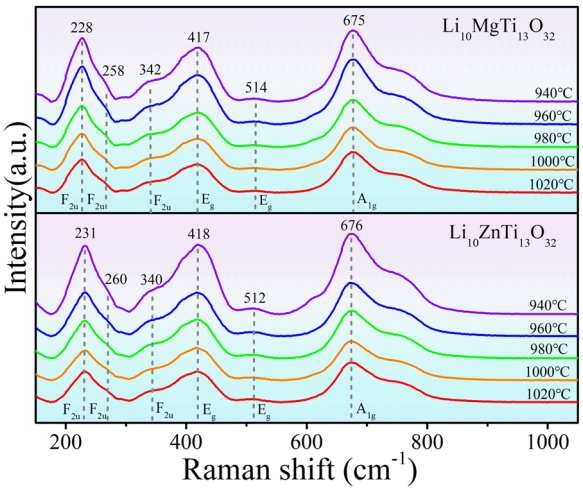

Fig. 2 Raman spectra of the $Li_{10}MTi_{13}O_{32}$ (M = Zn, Mg) ceramics studied at different sintering temperatures.

Table 2 Raman vibration modes the $Li_{10}MTi_{13}O_{32}$ (M = Zn, Mg) ceramics

$Li_{10}ZnTi_{13}O_{32}$	$Li_{10}MgTi_{13}O_{32}$		
Raman mode (cm^{-1})	Raman mode (cm^{-1})	Symmetry mode	Assignment
231	228	F_{2u}	O–Li–O, O–Ti–$O_{bending}$
258	260	F_{2u}	O–Li–O, O–Ti–$O_{bending}$
340	342	F_{2u}	O–Li–O, O–Ti–$O_{bending}$
418	417	E_g	$[LiO_4]_{stretching}$
514	512	E_g	$[Zn/MgO_4]_{stretching}$
676	675	A_{1g}	$[TiO_6]_{stretching}$

uniform and compact. When the temperature was raised further, the size of some grains increased abnormally. As shown in Fig. 3d–f, the grain growth process of the $Li_{10}MgTi_{13}O_{32}$ ceramic (the average grain size increased from 2.66 μm to 4.85 μm) is similar to that of $Li_{10}ZnTi_{13}O_{32}$, and the densest microstructure is obtained at 980 °C.

Fig. 4a presents the variation of the bulk density and relative density of the $Li_{10}MTi_{13}O_{32}$ (M = Zn, Mg) ceramics at different sintering temperatures. The theoretical density is calculated based on structural refinement (3.6009 g cm^{-3} for $Li_{10}ZnTi_{13}O_{32}$ and 3.4827 g cm^{-3} for $Li_{10}MgTi_{13}O_{32}$). Both $Li_{10}ZnTi_{13}O_{32}$ and $Li_{10}MgTi_{13}O_{32}$ show high relative densities (>95%) in the sintering range. The saturation relative density of $Li_{10}ZnTi_{13}O_{32}$ was 98.19% at 980 °C, and the maximum relative density of $Li_{10}MgTi_{13}O_{32}$ was 98.25%.

As shown in Fig. 4b, the ε_r of the $Li_{10}ZnTi_{13}O_{32}$ ceramic increases from 27.42 at 940 °C to 28.23 at 980 °C, after which it decreases slightly with increasing temperature, and the change in the ε_r of the $Li_{10}MgTi_{13}O_{32}$ ceramic is consistent with that of $Li_{10}ZnTi_{13}O_{32}$, reaching a maximum of 29.23 at 980 °C. In general, the relative permittivity of the ceramics is correlated with the porosity, which can be corrected using the Bosman–Havinga equation:[38]

$$\varepsilon_{r(corr)} = \varepsilon_r(1 + 1.5P) \quad (3)$$

$$P = 1 - \frac{\rho_{mea}}{\rho_{th}} \quad (4)$$

where P denotes the fractional porosity, and ρ_{th} and ρ_{mea} are the theoretical and measured density values, respectively. The corrected permittivity $\varepsilon_{r(corr)}$ at the optimum sintering temperature is 28.99 for $Li_{10}ZnTi_{13}O_{32}$ and 30.00 for the $Li_{10}MgTi_{13}O_{32}$ ceramic. The evaluated permittivity $\varepsilon_{r(C-M)}$ is 16.05 for $Li_{10}ZnTi_{13}O_{32}$ and 15.47 for $Li_{10}MgTi_{13}O_{32}$, which are calculated using the Clausius–Mossotti equation:[39]

$$\varepsilon_{r(C-M)} = \frac{3V_m + 8\pi\alpha_D}{3V_m - 4\pi\alpha_D} \quad (5)$$

$$\alpha_D = 10\alpha(Li^+) + \alpha(Zn/Mg^{2+}) + 13\alpha(Ti^{4+}) + 32\alpha(O^{2-}) \quad (6)$$

Here, α_D is the molecular dielectric polarizability, which is the sum of the dielectric polarizabilities of the individual ions: Li^+ (1.20 $Å^3$), Zn^{2+} (2.04 $Å^3$), Mg^{2+} (1.32 $Å^3$), Ti^{4+} (2.93 $Å^3$) and O^{2-} (2.01 $Å^3$). It is clear that $\varepsilon_{r(C-M)}$ is rather low compared with

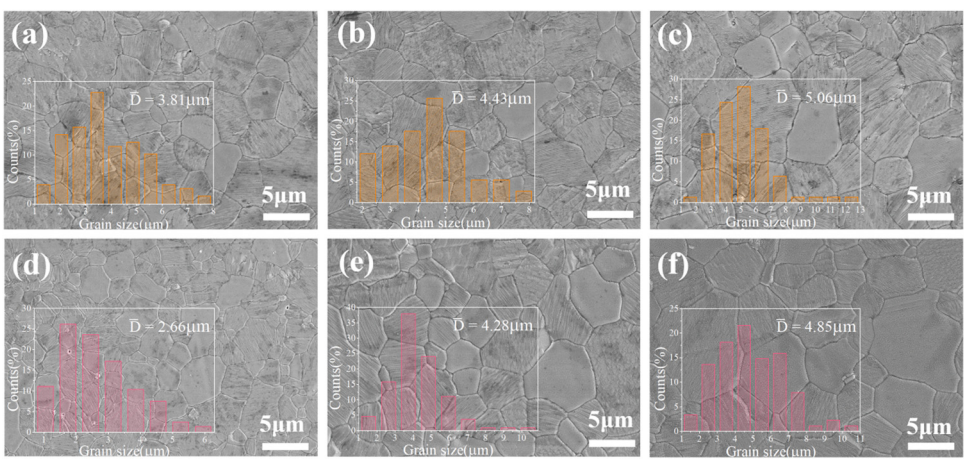

Fig. 3 Polished and thermally etched SEM images of the $Li_{10}ZnTi_{13}O_{32}$ ceramic sintered at (a) 940 °C, (b) 980 °C, and (c) 1020 °C, and the $Li_{10}MgTi_{13}O_{32}$ ceramic sintered at (d) 940 °C, (e) 980 °C, and (f) 1020 °C.

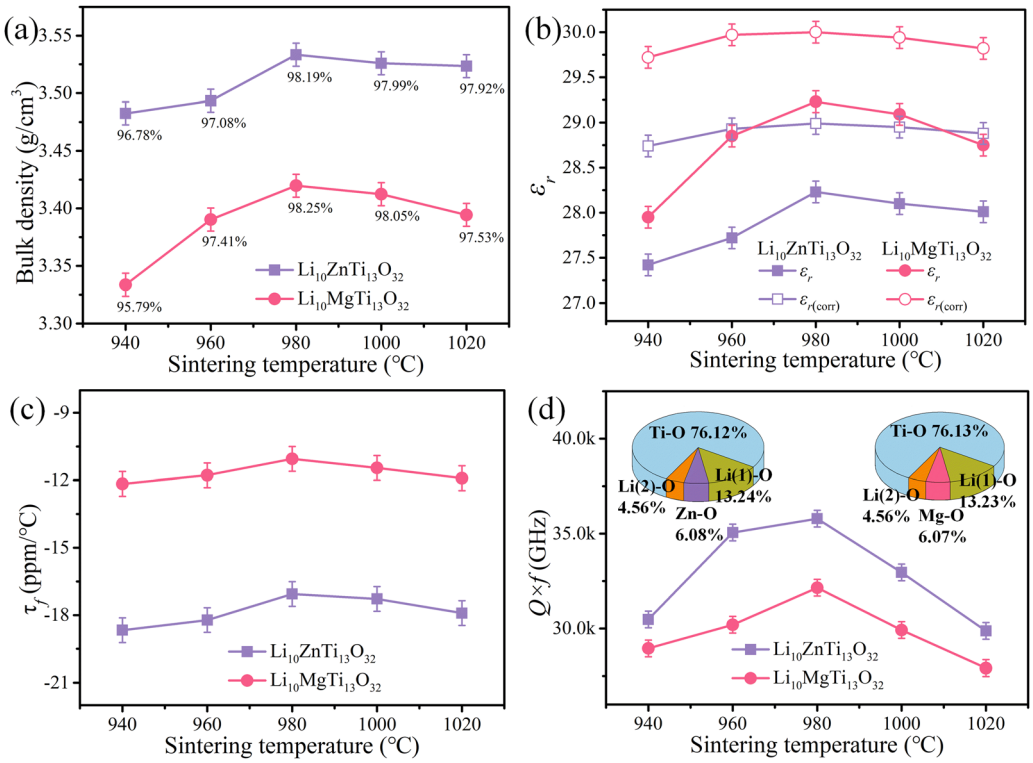

Fig. 4 (a) Density, (b) ε_r, (c) τ_f, and (d) $Q \times f$ of the $Li_{10}MTi_{13}O_{32}$ (M = Zn, Mg) samples as a function of the sintering temperature, the inset in (d) shows the contribution of each bond to the lattice energy.

$\varepsilon_{r(corr)}$, as listed in Table 3. In addition, the $\varepsilon_{r(corr)}$ of $Li_{10}MgTi_{13}O_{32}$ is larger than $Li_{10}ZnTi_{13}O_{32}$, an opposite trend to that of $\varepsilon_{r(C-M)}$. The discrepancy between $\varepsilon_{r(corr)}$ and $\varepsilon_{r(C-M)}$ can be due to the "rattling" or "compressed" cations. When the motion of cations and/or anions is restricted by crystal symmetry, larger than normal bond distances and/or thermal motions may occur, resulting in abnormally large polarizabilities.[40,41] Macroscopically, the variation in the bond length is manifested as the change in the bond valence (BV; V_i):

$$V_i = \sum_j V_{ij} \quad (7)$$

$$V_{ij} = \exp\left[\frac{R_{ij} - d_{ij}}{b}\right] \quad (8)$$

Where R_{ij} is the bond valence parameter, d_{ij} is the bond length and b is a constant (0.37 Å).[42] Table 4 presents the BV values of the $Li_{10}ZnTi_{13}O_{32}$ and $Li_{10}MgTi_{13}O_{32}$ ceramics. The average bond valence (1.0921 v.u.) of the A-site (8a) in $Li_{10}ZnTi_{13}O_{32}$ is slightly lower than the normal value (1.1250 v.u.), indicating that the A-site is in an expanded state and that both Li(1) and Zn are rattling cations. The B-site (16d) also shows an expanded state, but only Ti is a rattling cation, and Li(2) is tightly bound in its octahedral site and is not a rattling cation. The same is true for each ion in $Li_{10}MgTi_{13}O_{32}$. The weighted average discrepancy factor ($<d>$) can give the average deviation from the normal bond valence sums in a compound:

$$\langle d \rangle = \frac{\sum_i^n W_i D_i}{N} \quad (9)$$

where W is the Wyckoff site multiplicity, D_i is the discrepancy factor for each of the n ions on a distinct crystallographic site, and N is the number of atoms in the unit cell. As listed in Table 4, the negative $\langle d \rangle$ values of the $Li_{10}MTi_{13}O_{32}$ (M = Zn, Mg) ceramics indicate that the ions are, on average, underbonded and the overall structure of the material is in a slightly expanded state. The $\varepsilon_{r(corr)}$ is higher than $\varepsilon_{r(C-M)}$ because longer and weaker bonds are more likely to cause polarization. Furthermore, the $|<d>|$ value of $Li_{10}MgTi_{13}O_{32}$ (0.0670 v.u.) is slightly higher than that of $Li_{10}ZnTi_{13}O_{32}$ (0.0601 v.u.), which explains why, although $Li_{10}MgTi_{13}O_{32}$ has a lower α_D value than $Li_{10}ZnTi_{13}O_{32}$, its $\varepsilon_{r(corr)}$ value is slightly higher.

The bond ionicity (f_i) can be calculated using Phillips–Van Vechten–Levine (P–V–L) theory and structural refinement of the bond length (Table S1, ESI†), which is usually related to the variation of the measured ε_r.[43,44] The relationship between

Table 3 Permittivity and τ_f values of the $Li_{10}MTi_{13}O_{32}$ (M = Zn, Mg) ceramics at the optimal sintering temperature

Compounds	S.T. (°C)	ε_r	$\varepsilon_{r(corr)}$	$\varepsilon_{r(C-M)}$	$\Delta\varepsilon_r$ (%)	τ_f (ppm per °C)
$Li_{10}ZnTi_{13}O_{32}$	980	28.23 ± 0.3	28.99	16.05	80.62	−17.06 ± 2.0
$Li_{10}MgTi_{13}O_{32}$	980	29.23 ± 0.3	30.00	15.47	93.92	−11.05 ± 2.0

Table 4 Bond ionicity and bond valences of the $Li_{10}MTi_{13}O_{32}$ (M = Zn, Mg) ceramics

Compound	Atom	f_i^μ (%)	Site	BV (v.u.)	Average BV (v.u.)	Normal BV (v.u.)	D_i (v.u.)	$<d>$ (v.u.)
$[Zn_{0.125}Li_{0.875}]^{tet}[Li_{0.1875}Ti_{0.8125}]^{oct}O_4$	Zn(1)	43.2111	8a	1.8671	1.0921	1.1250	−0.1329	−0.0601
	Li(1)	65.7780		0.9813			−0.0187	
	Li(2)	66.9681	16d	1.4366	3.2672	3.4375	−0.5634	
	Ti(1)	92.8605		3.6897			−0.3103	
	O(1)		32e	2.0819	2.0819	2.0000	0.0819	
$[Mg_{0.125}Li_{0.875}]^{tet}[Li_{0.1875}Ti_{0.8125}]^{oct}O_4$	Mg(1)	43.2442	8a	1.8027	1.0794	1.1250	−0.1973	−0.0670
	Li(1)	65.8038		0.9760			−0.0240	
	Li(2)	66.9655	16d	1.4390	3.2725	3.4375	−0.5610	
	Ti(1)	92.8611		3.6957			−0.3043	
	O(1)		32e	2.0703	2.0703	2.0000	0.0703	

the bond ionicity (f_i) and ε_r can be described using the following formula:[45]

$$\varepsilon_r = \frac{n^2 - 1}{1 - f_i} + 1 \quad (10)$$

where n is the refractive index. The f_i of the μ bond is obtained using the following formula:[46]

$$f_i^\mu = \frac{(C^\mu)^2}{(E_g^\mu)^2} \quad (11)$$

where E_g^μ and C^μ are the average energy interval and heteropolar part, respectively (Table S2, ESI†). As listed in Table 4, the smaller bond ionicity of all the bonds in $Li_{10}ZnTi_{13}O_{32}$ is observed, suggesting a lower ε_r for $Li_{10}ZnTi_{13}O_{32}$ for than $Li_{10}MgTi_{13}O_{32}$. Besides, $f_{i(Ti-O)}^\mu$ possesses the maximum value in the $Li_{10}MTi_{13}O_{32}$ (M = Zn, Mg) ceramics, indicating that the Ti–O bond contributes the most to ε_r.

As shown in Fig. 4c, the τ_f values of the $Li_{10}MTi_{13}O_{32}$ (M = Zn, Mg) ceramics sintered at various temperatures show a weak temperature dependence and remained stable at around −17.06 ppm per °C ($Li_{10}ZnTi_{13}O_{32}$) and −11.05 ppm per °C ($Li_{10}MgTi_{13}O_{32}$). Generally, τ_f is strongly determined by the coefficient of thermal expansion (α_L) and the temperature coefficient of the dielectric constant (τ_ε) [*i.e.*, $\tau_f = -(\tau_\varepsilon/2 + \alpha_L)$].[47] The measured τ_ε values are +2.61 ppm per °C for $Li_{10}MgTi_{13}O_{32}$ and +15.77 ppm per °C for $Li_{10}ZnTi_{13}O_{32}$ at microwave frequencies between 25 °C and 85 °C. The α_L values of the $Li_{10}MgTi_{13}O_{32}$ and $Li_{10}ZnTi_{13}O_{32}$ ceramics are calculated as 9.74 ppm per °C and 9.18 ppm per °C, respectively. Clearly, τ_ε is larger than α_L and thus plays a dominant role in τ_f. And more deeply, τ_ε is related to the temperature coefficient of ionic polarizability ($\tau_{\alpha m}$):[48]

$$\tau_\varepsilon = \frac{1}{\varepsilon_r}\left(\frac{\partial \varepsilon_r}{\partial T}\right) = \frac{(\varepsilon_r - 1)(\varepsilon_r + 2)}{3\varepsilon_r}\left(\frac{1}{\alpha_m}\frac{d\alpha_m[T, V(T)]}{d\mathrm{T}} - 3\alpha_L\right) = \frac{(\varepsilon_r - 1)(\varepsilon_r + 2)}{3\varepsilon_r}(\tau_{\alpha m} - 3\alpha_L) \quad (12)$$

The $\tau_{\alpha m}$ values are 29.16 ppm per °C for $Li_{10}ZnTi_{13}O_{32}$ and 29.48 ppm per °C for $Li_{10}MgTi_{13}O_{32}$. Therefore, the negative τ_f values for $Li_{10}MTi_{13}O_{32}$ (M = Zn, Mg) originate from the positive $\tau_{\alpha m}$ value being slightly higher than $3\alpha_L$, which makes the τ_f values close to zero.

As shown in Fig. 4d, the maximum $Q \times f$ values of 35 800 and 32 100 GHz are obtained, respectively, for $Li_{10}ZnTi_{13}O_{32}$ and $Li_{10}MgTi_{13}O_{32}$ sintered at 980 °C. The $Q \times f$ of $Li_{10}MgTi_{13}O_{32}$ is slightly lower than that of $Li_{10}ZnTi_{13}O_{32}$, which may be due to the increase in intrinsic dielectric loss caused by weakly bonded cations in the extended coordination environment. In a classical sense, the more under-bonded cations contribute to the dielectric loss because the cations "rattle" more freely in the polyhedral cage and may interact more strongly with the anharmonic phonons.[49] For intrinsic losses, the lattice energy (U) based on P–V–L theory can be evaluated as follows:[50–52]

$$U_{total} = \sum_\mu \left(U_{bc}^\mu + U_{bi}^\mu\right) \quad (13)$$

$$U_{bc}^\mu = 2100m\frac{(Z_+^\mu)^{1.64}}{(d^\mu)^{0.75}}f_c^\mu \quad (14)$$

$$U_{bi}^\mu = 1270\frac{(m+n)Z_+^\mu Z_-^\mu}{d^\mu}\left(1 - \frac{0.4}{d^\mu}\right)f_i^\mu \quad (15)$$

where Z_+^μ and Z_-^μ are the valence states of the cation and anion, d^μ is the bond length, and U_{bi}^μ and U_{bc}^μ are the ionic part and the covalent part of the μ bond, respectively. As listed in Table 5, the total lattice energy (U_{total}) of the $Li_{10}ZnTi_{13}O_{32}$ ceramic is greater than that of the $Li_{10}MgTi_{13}O_{32}$ ceramic, and the larger U_{total} corresponds to the higher $Q \times f$ value. This is because the $Q \times f$ value is mainly determined by the lattice anharmonicity.[53] As the lattice energy increases, the lattice anharmonicity will also increase, which reduces the inherent dielectric loss and

Table 5 Bond length (d), lattice energy (U), $Q \times f$, and packing fraction of the $Li_{10}MTi_{13}O_{32}$ (M = Zn, Mg) ceramics

Ceramic	Bond type	d (Å)	U (kJ mol^{-1})	$Q \times f$ (GHz)	Packing fraction (%)
$Li_{10}ZnTi_{13}O_{32}$	Li(1)–O × 4	1.9859	913.4093	35 800 ± 500	68.42
	Zn–O × 4	1.9859	419.3192		
	Li(2)–O × 6	1.9949	314.7417		
	Ti–O × 6	1.9949	5250.0245		
	U_{total} = 6897.4947				
$Li_{10}MgTi_{13}O_{32}$	Li(1)–O × 4	1.9879	912.5777	32 100 ± 500	68.36
	Mg–O × 4	1.9879	418.9638		
	Li(2)–O × 6	1.9943	314.8187		
	Ti–O × 6	1.9943	5250.1225		
	U_{total} = 6897.4827				

Table 6 Variation of the FWHM value of the Raman spectrum with the sintering temperature for the $Li_{10}MTi_{13}O_{32}$ (M = Zn, Mg) ceramics

Compound	Sintering temperature (°C)	FWHM (cm^{-1})
$Li_{10}ZnTi_{13}O_{32}$	940	79.03337
	960	78.40893
	980	78.31708
	1000	78.53711
	1020	79.51513
$Li_{10}MgTi_{13}O_{32}$	940	75.12137
	960	74.89138
	980	74.47194
	1000	75.18652
	1020	76.04403

increases the $Q \times f$ value. Moreover, the lattice energy of the Ti–O bond is much greater than that of other bonds, accounting for 76.12% of the total lattice energy for $Li_{10}ZnTi_{13}O_{32}$ and 76.13% for $Li_{10}MgTi_{13}O_{32}$, indicating that the contribution of the Ti–O bond to the $Q \times f$ value is dominant. In addition, the $Q \times f$ value is strongly dependent on the packing fraction, which is defined by summing the volume of packed ions over the unit cell volume:[54]

$$\text{Packing fraction } (\%) = \frac{\text{volume of packed ions}}{\text{volume of unit cell}} \times Z \quad (16)$$

As seen in Table 5, the packing fraction of $Li_{10}ZnTi_{13}O_{32}$ (68.42%) is higher than that of $Li_{10}MgTi_{13}O_{32}$ (68.36%). The increase in packing fraction can reduce the vibration of the crystal lattice and thus enhance the quality factor. Raman spectroscopy is also an effective tool for studying lattice vibration information and dielectric loss.[55] Table 6 shows the FWHM values of the A_{1g} mode at different sintering temperatures for the $Li_{10}MTi_{13}O_{32}$ (M = Zn, Mg) ceramics, and the trend of $Q \times f$ is opposite to the FWHM. The lower the FWHM, the smaller the space for lattice vibration and the non-harmonic vibration, resulting in a decrease in the inherent dielectric loss or an increase in $Q \times f$.[56]

The $Q \times f$ values of the disordered spinel ($Fd\bar{3}m$) microwave dielectric ceramics $Li_{10}ZnTi_{13}O_{32}$ and $Li_{10}MgTi_{13}O_{32}$ are not as high as those of ordered spinels, which may be related to the transport of Li^+ ions in the structure. Complex impedance analysis was employed to explain the effects of Li^+ ions on the structure and $Q \times f$. Fig. 5a and b show the complex impedance plane plots of the $Li_{10}MTi_{13}O_{32}$ (M = Zn, Mg) ceramics at 633–573K. The $Li_{10}MTi_{13}O_{32}$ (M = Zn, Mg) ceramics show high resistivity and good insulation. The relationship between the DC (direct current) conductivity (σ_{dc}) and the temperature can be expressed *via* the following Arrhenius equation:

$$\sigma_{dc} = \sigma_0 \exp\left(\frac{-E_{dc}}{k_B T}\right) \quad (17)$$

where σ_0 is the pre-constant, k_B is the Boltzmann constant (8.617×10^{-5} eV K^{-1}), T is the temperature (in Kelvin), and E_{dc} is the activation energy from DC conductivity. The E_{dc} values for $Li_{10}MTi_{13}O_{32}$ (M = Zn, Mg) can be obtained according to the

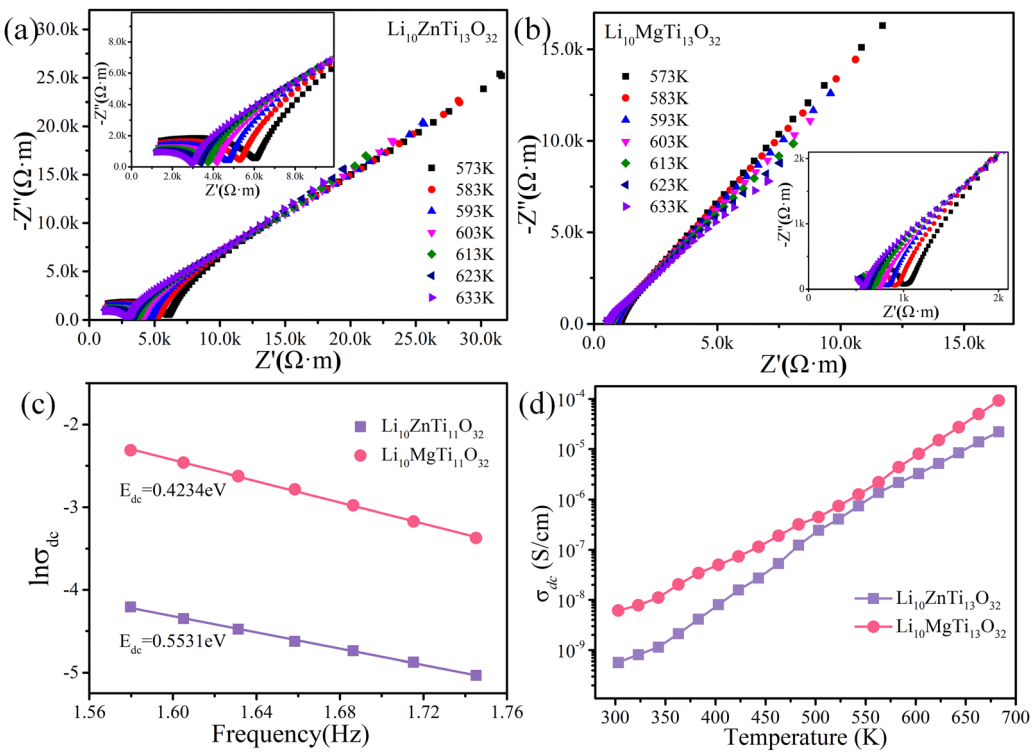

Fig. 5 Complex impedance plane plots of (a) $Li_{10}ZnTi_{13}O_{32}$ and (b) $Li_{10}MgTi_{13}O_{32}$ at 633–573 K. (The inset shows a magnification of the impedance). (c) Arrhenius plots of DC conductivity (σ_{dc}) for the $Li_{10}MTi_{13}O_{32}$ (M = Zn, Mg) ceramics. (d) DC conductivity of the $Li_{10}MTi_{13}O_{32}$ (M = Zn, Mg) ceramics as a function of temperature.

slope of the fitted straight line for each ceramic: E_{dc} = 0.4230 eV for $Li_{10}ZnTi_{13}O_{32}$, and E_{dc} = 0.5531 eV for $Li_{10}MgTi_{13}O_{32}$ (Fig. 5c). The DC conductivity activation energy can reflect the sum of the free energies of the carriers to produce long jumps, and the small E_{dc} values in the $Li_{10}MTi_{13}O_{32}$ (M = Zn, Mg) ceramics might come from the embedding and detaching of Li^+ in the spinel structure. The DC conductivities of the $Li_{10}MTi_{13}O_{32}$ (M = Zn, Mg) ceramics as a function of temperature were also measured in Fig. 5d. When the temperature is increased from 303 K to 683 K, the conductivity of $Li_{10}ZnTi_{13}O_{32}$ increases from 5.67 × 10^{-10} S cm^{-1} to 2.21 × 10^{-5} S cm^{-1}, and the conductivity of $Li_{10}MgTi_{13}O_{32}$ increases from 6.11 × 10^{-9} S cm^{-1} to 9.27 × 10^{-5} S cm^{-1}, where the conductivity of $Li_{10}ZnTi_{13}O_{32}$ is less than that of $Li_{10}MgTi_{13}O_{32}$. Li-rich spinel materials are also candidates for lithium-ion conductors, such as $Li_4Ti_5O_{12}$, which brings about the higher dielectric loss of this material relative to other spinels.

4. Conclusions

$Li_{10}MTi_{13}O_{32}$ (M = Zn, Mg) ceramics with a disordered spinel structure ($Fd\bar{3}m$) were synthesized using a solid-state reaction method. $Li_{10}ZnTi_{13}O_{32}$ and $Li_{10}MgTi_{13}O_{32}$ with relative permittivities of 28.23 ± 0.3 and 29.23 ± 0.3, $Q \times f$ values of 35 800 ± 500 GHz and 32 100 ± 500 GHz (at ~7.5 GHz), and τ_f values of −17.06 ± 2.0 ppm per °C and −11.05 ± 2.0 ppm per °C, respectively, were obtained at 980 °C. The permittivities $\varepsilon_{r(C-M)}$ calculated using the Clausius–Mossotti (C–M) equation are significantly lower than the permittivities $\varepsilon_{r(corr)}$ corrected by the porosity ($\varepsilon_{r(C-M)}$ = 16.05, $\varepsilon_{r(corr)}$ = 28.99 for $Li_{10}ZnTi_{13}O_{32}$; $\varepsilon_{r(C-M)}$ = 15.47, $\varepsilon_{r(corr)}$ = 30.00 for $Li_{10}MgTi_{13}O_{32}$). The main reason for this phenomenon comes from the longer and weaker bonds in the $Li_{10}MTi_{13}O_{32}$ (M = Zn, Mg) ceramics that are more facile to polarization. The larger negative weighted average discrepancy factor ($<d>$) of $Li_{10}MgTi_{13}O_{32}$ (−0.0670 v.u.) than that of $Li_{10}ZnTi_{13}O_{32}$ (−0.0601 v.u.) is a good explanation for the higher $\varepsilon_{r(corr)}$ value of $Li_{10}MgTi_{13}O_{32}$ (α_D = 115.73 A^3), although its dielectric polarizability (α_D) is lower than that of $Li_{10}ZnTi_{13}O_{32}$ (α_D = 116.45 A^3). This expansion structure also results in a closer value of τ_f to zero and a lower $Q \times f$. Values of the temperature coefficient of ionic polarizability ($\tau_{\alpha m}$) are 29.22 ppm per °C for $Li_{10}ZnTi_{13}O_{32}$ and 29.84 ppm per °C for $Li_{10}MgTi_{13}O_{32}$, and the small negative τ_f values of $Li_{10}MTi_{13}O_{32}$ (M = Zn, Mg) are derived from the proximity of $\tau_{\alpha m}$ to $3\alpha_L$. Calculations using P–V–L theory also confirmed that the bond ionicity (f_i) of all the bonds in the prepared $Li_{10}MgTi_{13}O_{32}$ structure was higher than that of $Li_{10}ZnTi_{13}O_{32}$, and the Ti–O bond contributed the most to ε_r. The lattice energy of the Ti–O bonds is much greater than that of other bonds, indicating that it is also a major contributor to $Q \times f$ in the $Li_{10}MTi_{13}O_{32}$ (M = Zn, Mg) ceramics. In addition, a study of the DC conductivity clarified that the $Q \times f$ values of the disordered spinels $Li_{10}ZnTi_{13}O_{32}$ and $Li_{10}MgTi_{13}O_{32}$ are not as high as other ordered spinels, which may be due to the transport of Li^+ ions in their structures.

Conflicts of interest

There are no conflicts to declare.

Acknowledgements

This work was supported by the National Natural Science Foundation of China (No. 22105048), Guangxi Science and Technology Plan Project (No. AD20297035), the Natural Science Foundation of Guangxi Zhuang Autonomous Region (No. 2022GXNSFBA035602), the Guilin University of Technology Research Startup Project (No. GUTQDJJ2021073), and the Guangxi BaGui Scholars Special Funding.

References

1 C. L. Huang and T. H. Hsu, *J. Eur. Ceram. Soc.*, 2022, **42**, 3892–3897.
2 J. Li, J. Zhu and G. Wang, *Ceram. Int.*, 2022, **48**, 15261–15267.
3 S. Z. Hao, D. Zhou, L. X. Pang, M. Z. Dang, S. K. Sun, T. Zhou, S. Trukhanov, A. Trukhanov, A. S. B. Sombra, Q. Li, X. Q. Zhang, S. Xia and M. A. Darwish, *J. Mater. Chem. C*, 2022, **10**, 2008–2016.
4 J. Bao, Y. Zhang, H. Kimura, H. Wu and Z. Yue, *J. Adv. Ceram.*, 2023, **12**, 82–92.
5 X. Zhou, L. Liu, J. Sun, N. Zhang, H. Sun, H. Wu and W. Tao, *J. Adv. Ceram.*, 2021, **10**, 778–789.
6 H. Tian, J. Zheng, L. Liu, H. Wu, H. Kimura, Y. Lu and Z. Yue, *J. Mater. Sci. Technol.*, 2022, **116**, 121–129.
7 T. Y. Qin, C. W. Zhong, Y. Shang, L. Cao, M. X. Wang, B. Tang and S. R. Zhang, *J. Alloys Compd.*, 2021, **886**, 161278.
8 K. P. Surendran, P. V. Bijumon, P. Mohanan and M. T. Sebastian, *Appl. Phys. A: Mater. Sci. Process.*, 2005, **81**, 823–826.
9 S. Takahashi, Y. Imai, A. Kan, Y. Hotta and H. Ogawa, *Jap. J. Appl. Phys.*, 2015, **54**, 10NE02.
10 A. Belous, O. Ovchar, D. Durilin, M. M. Krzmanc, M. Valant and D. Suvorov, *J. Am. Ceram. Soc.*, 2006, **89**, 3441–3445.
11 H. F. Zhou, X. L. Chen, L. Fang, D. J. Chu and H. Wang, *J. Mater. Res.*, 2010, **25**, 1235–1238.
12 S. George and M. T. Sebastian, *J. Am. Ceram. Soc.*, 2010, **93**, 2164–2166.
13 L. Y. Ao, Y. Tang, J. Li, W. S. Fang, L. Duan, C. X. Su, Y. H. Sun, L. J. Liu and L. Fang, *J. Eur. Ceram. Soc.*, 2020, **40**, 5498–5503.
14 S. Takahashi, A. Kan and H. Ogawa, *Jap. J. Appl. Phys.*, 2016, **55**, 10TE01.
15 H. Zhou, X. Liu, X. Chen, L. Fang and Y. Wang, *J. Eur. Ceram. Soc.*, 2012, **32**, 261–265.
16 H. F. Zhou, J. Z. Gong, N. Wang and X. L. Chen, *Ceram. Int.*, 2016, **42**, 8822–8825.
17 N. Wang, H. F. Zhou, J. Z. Gong, G. C. Fan and X. L. Chen, *J. Electron. Mater.*, 2016, **45**, 3157–3161.
18 J. Zhang, R. Z. Zuo, Y. Wang and S. S. Qi, *Mater. Lett.*, 2016, **164**, 353–355.
19 H. Xiang, L. Fang, W. Fang, Y. Tang and C. Li, *J. Eur. Ceram. Soc.*, 2017, **37**, 625–629.

20 K. Xiao, Y. Tang, Y. F. Tian, C. C. Li, L. Duan and L. Fang, *J. Eur. Ceram. Soc.*, 2019, **39**, 3064–3069.
21 W. S. Fang, Y. M. Sun, L. Fang, Y. Tang and C. C. Li, *J. Alloys Compd.*, 2017, **722**, 1002–1007.
22 S. K. Singh, S. R. Kiran and V. R. K. Murthy, *Mater. Chem. Phys.*, 2013, **141**, 822–827.
23 R. Z. Zuo and J. Zhang, *J. Am. Ceram. Soc.*, 2016, **99**, 3343–3349.
24 H. Luo, L. Fang, H. Xiang, Y. Tang and C. Li, *Ceram. Int.*, 2017, **43**, 1622–1627.
25 L. Fang, D. Chu, H. Zhou, X. Chen and Z. Yang, *J. Alloys Compd.*, 2011, **509**, 1880–1884.
26 M. Li, Y. Tang, H. Xiang, J. Li, D. Zhou and L. Fang, *Ceram. Int.*, 2023, DOI: **10.1016/j.ceramint.2022.11.021**.
27 Y. Tang, H. Li, J. Li, W. Fang, Y. Yang, Z. Zhang and L. Fang, *J. Eur. Ceram. Soc.*, 2021, **41**, 7697–7702.
28 Y. Yang, Y. Tang, J. Li, L. Fang and H. C. Xiang, *ACS Appl. Electron. Mater.*, 2022, **4**, 3512–3519.
29 X. W. Hu, J. W. Chen, J. Li, H. C. Xiang, Y. Tang and L. Fang, *J. Eur. Ceram. Soc.*, 2022, **42**, 7461–7467.
30 Y. M. Dai, J. W. Chen, Y. Tang, H. C. Xiang, J. Li and L. Fang, *Ceram. Int.*, 2023, **49**, 875–881.
31 V. S. Hernandez, L. M. T. Martinez, G. C. Mather and A. R. West, *J. Mater. Chem.*, 1996, **6**, 1533–1536.
32 L. T. Nong, X. F. Cao, C. C. Li, L. J. Liu, L. Fang and J. Khaliq, *J. Eur. Ceram. Soc.*, 2021, **41**, 7683–7688.
33 H. D. Lutz, *Z. Naturforsch., A: Phys. Sci.*, 1969, **24**, 1417–1419.
34 D. Z. Liu, W. Hayes, M. Kurmoo, M. Dalton and C. Chen, *Phys. C*, 1994, **235**, 1203–1204.
35 H. D. Lutz, B. Müller and H. J. Steiner, *J. Solid State Chem.*, 1991, **90**, 54–60.
36 L. Malavasi, P. Galinetto, M. C. Mozzati, C. B. Azzoni and G. Flor, *Phys. Chem. Chem. Phys.*, 2002, **4**, 3876–3880.
37 A. Magrez, M. Cochet, O. J oubert, G. Louarn, M. Ganne and O. Chauvet, *Chem. Mater.*, 2001, **13**, 3893–3898.
38 A. J. Bosman and E. E. Havinga, *Phys. Rev.*, 1963, **129**, 1593–1600.
39 R. D. Shannon, *J. Appl. Phys.*, 1993, **73**, 348–366.
40 H. S. Park, K. H. Yoon and E. S. Kim, *Mater. Chem. Phys.*, 2003, **79**, 181–183.
41 Y. S. Cho, K. H. Yoon, B. D. Lee, H. R. Lee and E. S. Kim, *Ceram. Int.*, 2004, **30**, 2247–2250.
42 N. E. Brese and M. O. Keeffe, *Acta Crystallogr.*, 1991, **47**, 192–197.
43 H. Y. Yang, S. R. Zhang, H. C. Yang, Y. Yuan and E. Z. Li, *J. Am. Ceram. Soc.*, 2019, **102**, 5365–5374.
44 H. Y. Yang, S. R. Zhang, H. C. Yang and E. Z. Li, *Inorg. Chem. Front.*, 2020, **7**, 4711–4753.
45 S. S. Batsanov, *Russ. Chem. Rev.*, 1982, **51**, 684–697.
46 B. F. Levine, *J. Chem. Phys.*, 1973, **59**, 1463–1486.
47 E. L. Colla, I. M. Reaney and N. Setter, *J. Appl. Phys.*, 1993, **74**, 3414–3425.
48 A. J. Bosman and E. E. Havinga, *Phys. Rev.*, 1963, **129**, 1593.
49 M. W. Lufaso, *Chem. Mater.*, 2004, **16**, 2148–2156.
50 H. Yang, S. Zhang, Y. Chen, H. Yang, Y. Yuan and E. Li, *Inorg. Chem.*, 2019, **58**, 968–976.
51 D. Liu, S. Zhang and Z. Wu, *Inorg. Chem.*, 2003, **42**, 2465–2469.
52 R. Zurmühlen, J. Petzelt, S. Kamba, V. V. Voitsekhovskii, E. Colla and N. Setter, *J. Appl. Phys.*, 1995, **77**, 5341–5350.
53 Y. G. Zhao and P. Zhang, *RSC Adv.*, 2015, **5**, 97746–97754.
54 B. D. Silverman, *J. Phys. Rev.*, 1962, **125**, 1921–1930.
55 S. Y. Wang, J. D. Chen, Y. J. Zhang and Y. C. Zhang, *J. Alloys Compd.*, 2019, **805**, 852–858.
56 Y. Tang, S. Y. Shen, J. Li, X. G. Zhao, H. C. Xiang, H. P. Su, D. Zhou and L. Fang, *J. Eur. Ceram. Soc.*, 2022, **42**, 4573–4579.